HHS Public Access

Author manuscript

Clin Cancer Res. Author manuscript; available in PMC 2021 January 01.

Published in final edited form as:

Clin Cancer Res. 2020 July 01; 26(13): 3431–3442. doi:10.1158/1078-0432.CCR-19-1627.

Generation of genetically engineered mouse lung organoid models for squamous cell lung cancers allows for the study of combinatorial immunotherapy

Josephine Hai[1,*], **Hua Zhang**[1,2], **Jin Zhou**[1], **Zhong Wu**[1], **Ting Chen**[1,2], **Eleni Papadopoulos**[2], **Catriona M. Dowling**[2], **Val Pyon**[2], **Yuanwang Pan**[2], **Jie Bin Liu**[1], **Roderick T. Bronson**[3], **Heather Silver**[2], **Patrick H. Lizotte**[1,4], **Jiehui Deng**[1,2], **Joshua Campbell**[1,5], **Lynette M. Sholl**[6], **Christine Ng**[7], **Ming-Sound Tsao**[7], **Cassandra Thakurdin**[2], **Adam J. Bass**[1,*], **Kwok-Kin Wong**[1,2,*]

[1]Department of Medical Oncology, Dana-Farber Cancer Institute, Boston, MA, USA

[2]Perlmutter Cancer Center, NYU Langone Medical Center, New York, NY, USA

[3]Rodent Histopathology, Harvard Medical School, Boston, MA, USA

[4]Belfer Center for Applied Cancer Science, Boston, MA, USA

[5]Department of Medicine, Boston University School of Medicine, Boston, MA, USA

[6]Department of Pathology, Brigham and Women's Hospital, Boston, MA, USA

[7]Princess Margaret Cancer Centre, University Health Network, Toronto, ON, Canada

Abstract

Purpose—Lung squamous cell carcinoma (LSCC) is a deadly disease for which only a subset of patients responds to immune checkpoint blockade (ICB) therapy. Therefore, preclinical mouse models that recapitulate the complex genetic profile found in patients are urgently needed.

Experimental Design—We used CRISPR genome editing to delete multiple tumor suppressors in lung organoids derived from Cre-dependent SOX2 knock-in mice. We investigated both the therapeutic efficacy and immunological effects accompanying combination PD-1 blockade and WEE1 inhibition in both mouse models and LSCC patient-derived cell lines.

Results—We show that multiplex gene editing of mouse lung organoids using the CRISPR-Cas9 system allows for efficient and rapid means to generate LSCCs that closely mimic the human disease at the genomic and phenotypic level. Using this genetically-defined mouse model and three-dimensional tumoroid culture system, we show that WEE1 inhibition induces DNA damage that primes the endogenous type I interferon and antigen presentation system in primary LSCC

Corresponding Authors: Dr. Kwok-Kin Wong, NYU Langone Medical School, 160 East 34th Street, New York, NY 10016. 212-263-5466. Kwok-Kin.Wong@nyumc.org, Dr. Adam J. Bass, Dana-Farber Cancer Institute, 450 Brookline Ave, Boston, MA 02215. 617-632-5707. adam_bass@dfci.harvard.edu, Dr. Josephine Hai, Dana-Farber Cancer Institute, 450 Brookline Ave, Boston, MA 02215. 617-582-8418. josephinehai@gmail.com.

*co-corresponding authors

Ethics approval:

All animal experiments were performed in accordance with procedures approved by the DFCI Animal Care and Use Committee.

tumor cells. These events promote cytotoxic T cell-mediated clearance of tumor cells and reduce the accumulation of tumor-infiltrating neutrophils. Beneficial immunological features of WEE1 inhibition are further enhanced by the addition of anti-PD-1 therapy.

Conclusions—We developed a mouse model system to investigate a novel combinatory approach that illuminates a clinical path hypothesis for combining ICB with DNA damage-inducing therapies in the treatment of LSCC.

Introduction

There are limited lung squamous cell carcinoma (LSCC) mouse models that recapitulate the co-occurring human LSCC mutations in genes encoding proteins operative in TP53, SOX2, PI3K and P16(INK4a) pathways. The study of cancer genes in mouse models has traditionally relied on genetically engineered strains made via gene targeting in embryonic stem cells. Such models take months to years to establish and require complicated breeding strategies when multiple genetic alterations are needed. Moreover, unlike human lung adenocarcinomas harboring *EGFR*-activating mutations or *ALK* fusions, for which targeted inhibitors have achieved objective responses in up to 80% cases, no targeted therapies currently exist for LSCC patients. The extent to which LSCC mutations in these pathways contribute to tumorigenesis, shape the tumor microenvironment, and affect therapeutic responses remains unclear. Here we describe a new rapid approach using a CRISPR/Cas9 genome multi-editing system in lung organoids derived from adult transgenic mice to generate an immunocompetent syngeneic mouse model that furthers rational immunotherapeutic options for LSCC.

Targeting tumor immune suppression pathways represents a paradigm shift in the treatment of lung cancer, which is the second most common cancer type in the United States. Despite the promising clinical activity of immune checkpoint blocking antibodies against programmed cell death protein 1/programmed death-ligand 1(PD-1/PD-L1) for non-small cell lung cancer (NSCLC), only a minority of patients (~20%) show a durable response (1). Thus, there is an urgent need to improve objective response rates. One strategy is to combine anti-PD-1 (pembrolizumab) with chemotherapy, which has been approved for first-line treatment of squamous NSCLC patients (2). Increasing evidence suggests that chemotherapy leads to immunological effects such as reduced T-regulatory cell activity, induced PD-L1 tumor expression and enhanced cross-presentation of tumor antigens (3, 4). Chemotherapeutic efficacy relies on DNA double-stranded break (DSB) formation followed by inflammatory cytokine production to drive the killing of tumor cells over several division cycles (5). Cyclin-dependent kinases 1 (CDK1) are fundamental drivers of the cell cycle G_2/M checkpoint and are required for the progression of various cancers (5, 6). We and others have previously demonstrated that interference with the CDK1 negative regulator WEE1 via a selective small-molecule WEE1 kinase inhibitor activates CDK1, which potently induces DSB formation due to loss of control at the G_2/M checkpoint, leading to lung cancer cell death (6). Previous studies have also shown that CDK1 can activate STAT1 signaling during mitosis, increasing pro-inflammatory cytokine production (5). We hypothesized that dual targeting of tumor cell-intrinsic (WEE1 inhibition) and immune cell-

intrinsic (anti-PD-1) pathways may potentiate superior anti-tumor activity compared with monotherapies.

Here we show that CDK1 activation via WEE1 inhibition induces DNA damage that primes the endogenous type I interferon and antigen presentation system in primary mouse and human LSCC tumor cells. We show in two mouse models, including our novel organoid-derived LSCC model, that WEE1 inhibition can enhance the anti-tumor activity of anti-PD-1 monotherapy by promoting cytotoxic NK cell-mediated clearance of tumor cells and decreasing immune-suppressive neutrophilic tumor infiltration.

Materials and Methods

Generation of SOX2; Cas9 mice

All mice used in this study were housed in the pathogen-free animal facilities in Dana Farber Cancer Institute (Boston, MA). The Rosa26R-lox-stop-lox-Sox2-IRES-GFP mice (hereafter referred as SOX2) have been described previously (7) and was generously gifted by Dr. Keith Ligon's laboratory (Boston, MA). The Hipp11-lox-stop-lox-Cas9 (hereafter referred as Cas9) mice were backcrossed to C57BL/6 background (Jackson Laboratory) and then bred with SOX2 to obtain a SOX2;Cas9 colony. All breeding and care procedures were approved by the Dana Farber Animal Care and Use Committee (Protocol number: 09–073) and carried out in strict accordance with the recommendations in the Guide for the Care and Use of Laboratory Animals of the National Institutes of Health.

Isolation and culturing of epithelial organoids from murine trachea and lung

After rinsing the dissected mouse lung with Hank's Salt (HBSS) supplemented with Gibco® antibiotic-antimycotic, we opened the main bronchi, placed the tissue in 1ml of dispase and incubated the tissue in a thermomixer for 15 minutes at 37ºC. We next peeled the epithelia from the submucosa and incubated the epithelia in 1ml of 0.25% trypsin-EDTA at 37ºC for 10 minutes, briefly vortexed, rinsed the tissue with 8mL of soybean trypsin inhibitor and repeated the trypsinization and wash cycle once more. We filtered the dissociated tissue through a 40μm cell strainer using PBS and centrifuged the cells at 200g for 5 minutes before resuspending the cells in organoid media (advanced DMEM/F12 media supplemented with Glutamax, 0.15mM HEPES, Gibco® antibiotic-antimycotic, N2 Supplement, B27 supplement, 1μM N-Acetylcysteine, 50ng/ml human EGF, and 3% conditioned media from L-WRN cells containing Wnt3a, Noggin, and R-spondin). Using a 1:1 ratio of organoid media and growth factor reduced basement membrane matrix (Matrigel, Corning), epithelial organoids were maintained for successive passages (>30 passages) by hanging drop method. For subsequent passages, organoids were dissociated by incubation in 0.25% trypsin. The trypsinization process disrupted the spherical organoids into cell aggregates that were then embedded in fresh Matrigel.

Cell culture and reagents

Human embryonic kidney (HEK293T) cells, BEAS2B cells and LSCC cell lines (NCI-H157, NCI-H226 and NCI-H520) were obtained from the American Type Culture Collection (ATCC). ATCC cells were cultured in either DMEM and RPMI1650 supplemented with

10% Fetal Bovine Serum (FBS) and antibiotics. The primary cultures of normal human bronchial epithelial HBE4 cells were previously derived (Table S1) and cultured in keratinocyte serum free (KSF) medium (Gibco-brl). Patient-derived xenografts were established from resected primary lung cancer without prior systemic therapy. Lung squamous carcinoma was confirmed by histology and p40 immunohistochemistry, a diagnostic marker for carcinoma of squamous lineage. All patients provided written consent and all patient-derived xenograft (PDX) cell lines (PDX139, 267 and 277) were previously derived using protocols approved by the University Health Network Human Research Ethics and Animal Care Committee (8). *KRAS, EGFR* and *PIK3CA* mutation status for PDX cell lines were detected using the Sequenom OncoCarta panel v1.0 as previously described (8) and on Table S1. All cell lines were authenticated by short-tandem repeat fingerprinting and mycoplasma tested by PCR.

LentiCRISPRv2 vector was obtained from Addgene (#52961). The *cre*-recombinase gene was first subcloned to replace the *Sp*Cas9 gene under the EFS promoter. Guide RNAs (gRNA) against mouse *PTEN*, *CDKN2A/p16* and *TP53* and E.coli *LacZ* gene were cloned into our modified lentiCRISPRv2-Cre vector and sequence verified (Table S2). Lentiviral pLKO.1 vector containing shRNAs targeting WEE1 (TRCN0000226425 and TRCN0000226426) were purchased from Sigma-Alrich. Transient transfections and virus preparation in HEK293T cells were performed using Fugene reagents (Promega) as per manufacturer's protocol. Lentivirus were prepared by transfecting two packaging plasmids into 293T cells using protocols from The RNAi Consortium (TRC; Broad Institute).

Organoids were isolated by digesting the Matrigel with 0.25% trypsin-EDTA in culture plates for 5–10 minutes at 37ºC and washed twice with PBS. Once organoids were dissociated, cells were pelleted and resuspended in 250μl lentiviral solution. Spinoculation was performed by transferring the suspension onto a 48-well plate and centrifuging the plate at 600g for one hour at 32ºC. Plates were then incubated at 37ºC for 6 hours before washing the suspension with fresh media and pelleting the cells to be embedded in fresh Matrigel media mixture by hanging drop method. Stable organoid cultures were selected by puromycin antibiotics (1–2μg/mL).

Drugs were obtained commercially: AZD1775 (HY-10993, MedChemExpress), PD0166285 (HY-13925; MedChemExpress), Wee1_II (CAS 622855–50-9, Calbiochem), BX-795 (SML0694, Sigma-Aldrich), Carboplatin (NYU Pharmacy), *In Vivo*MAb anti-mouse IFNAR-1 (clone MAR1–5A3, Bio X Cell) and anti-mouse CD8a (clone 53–6.7, Bio X Cell). Anti-mouse IgG2a and anti-mouse PD-1 (29F.1A12) was generously gifted by Dr. Gordon Freeman Laboratory (DFCI, Boston).

JH715 and JH716 mouse models

Organoids (2×10^6) were suspended in media, mixed with growth factor reduced Matrigel (Corning) at 1:1 ratio, and subcutaneously injected into female nude mice (Nu/Nu; Charles River Laboratories) in a final volume of 100μL. Length and width were measured twice a week using calipers. Tumor volumes were calculated using the formula (Length × Width^2)/2. All primary tumor cell lines were harvested from ~150–300mm^3 tumors, minced and digested in 4% collagenase for 30 minutes to 1 hour, then filtered through a 70 μM cell

strainer. Cell lines derived from mouse primary tumors were grown in advanced DMEM/F12 media supplemented with Glutamax (Invitrogen) supplemented with 10% FBS (Thermo Fisher) and antibiotics. Serial passage of tumor cell lines *in vivo* was performed by subcutaneous implantation into the flank of female C57BL/6 mice (Jackson Laboratory) and harvested as described above. All mice included in the survival analysis were euthanized when criteria for disease burden were reached or when targeted analysis end points were reached.

Animal treatment studies

C57BL/6 and DBA/2J mice were obtained from Jackson Laboratory and subcutaneously inoculated with JH716 (3×10^6) and KLN205 (0.5×10^6) cells in the right flank of 7 to 8-week-old mice. Mice were examined every 3–4 days, and tumor length and width were measured using calipers. Tumor volumes were calculated using the formula (Length × Width^2)/2. When tumor size reached a mean ~150 or 300mm^3, mice were randomly stratified to treatment arms: vehicle, AZD1775 (20mg/kg), anti-PD-1 (200μg), anti-CD8a (200ug), carboplatin (40mg/kg) or combination therapies. JH716 mice were treated up to 30 days, while KLN205 mice were treated up to 16 days. All manipulations were performed under sterile conditions in a laminar flow hood, in accordance with procedures approved by the DFCI Animal Care and Use Committee. At sacrifice, portions of tumors were snap-frozen and stored in liquid nitrogen or were fixed in 10% buffered formalin for routine histopathologic processing.

Immunohistochemistry

Samples resected from mice were fixed in 10% formalin, and then stored in 70% ethanol before processing and embedding. Immunohistochemistry was conducted on 5 micron sections. Tissue sections were deparaffinized, rehydrated and boiled for 15 minutes with a pressure cooker in 10mM pH6.0 Citrate buffer. Slides were incubated in 3% hydrogen peroxide for 30 minutes and then blocked in serum for one hour. Primary antibodies were added to the section and incubated overnight at 4°C (Table S3). Representative sections of human and mouse lung tumors were reviewed by independent pathologists including a rodent pathologist with expertise in mouse lung pathology (RB). Patient slides were obtained from the Brigham and Women's Hospital Department of Pathology under the Institutional Review Board protocol 2014P001715 and reviewed by a pathologist (LS).

Tumor-infiltrating immune cell isolation and flow cytometry analysis

Tumor-bearing mice were sacrificed and tumors were minced and digested in collagenase D and DNase I in Hank's Balanced Salt Solution (HBSS) at 37°C for 30 minutes. After incubation, the digested tissue was filtered through a 70μm cell strainer to obtain single-cell suspensions. Separated cells were treated with 1x RBC lysis buffer (Biolegend) to lyse red blood cells. Live cells were determined by LIVE/DEAD fixable Aqua dead cell stain kit (Molecular Probes). Cells were resuspended in PBS with 2% FBS for fluorescence-activated cell sorting (FACS) analysis. Cells were stained with antibodies listed in Table S3 followed by fixation/permeablization (Biolegend). Cells were imaged on LSR Fortessa (BD Biosciences) and analyzed with Flowjo software (Tree Star) using gating strategies shown in Figure S9.

Cytokine profiling of tumor lysates and conditioned media

Multiplex assays were performed on the EMD Millipore mouse cytokine/chemokine 32-plex panel (MCYTOMAG-70K) utilizing the bead-based immunoassay approach. Conditioned media from *ex vivo* 3D cultures were assayed neat. Mouse tumors were lysed in RIPA lysis buffer and protein levels were normalized in assays. Fold changes (FC) relative to the vehicle-treated tumors/matrigel alone media were calculated and plotted as $\log_2$FC. Lower and upper limits of quantitation (LLOQ/ULOQ) were imputed from standard curves for cytokines above or below detection.

Ex vivo culture systems

Mouse tumoroids were processed and loaded onto microfluidic devise as previously described (9). Live/Dead dual labeling was performed by loading microfluidic devise with AO/PI Staining Solution (CS2–0106, Nexcelom). After 20 minute dye incubation at room temperature, images were captured on a Nikon Eclipse 80i fluorescence microscope equipped with Z-stack (Prior) and CoolSNAP CCD camera (Roper Scientific). Image capture and analysis was performed using NIS-Elements AR software. Live and dead cell quantification was performed by measuring total cell area of each dye.

For 3D cell viability assays, tumoroids (40–100μm) were filtered by cell strainers and embedded in 1:1 growth factor reduced Matrigel:media and seeded in 96-well spheroid microplates (Fisher Scientific) forming a hanging drop. Cell viability was measured at 7 days using CellTiter-Glo® 3D (Promega) and the data was represented as the mean luminescence reading of 5–10 technical replicates relative to controls. Assays were repeated three times.

Results

Generation of CRISPR-mutant organoids gives rise to lung squamous carcinoma

SOX2 is the most frequently amplified gene in LSCC (7). Lu *et al.* previously demonstrated that SOX2 acts as an oncogene in transgenic mouse models conditionally overexpressing SOX2 alone in the lung; however, penetrance in this model was only 50% and pathology of resulting tumors were lung adenocarcinoma (7). Reasoning that multiple genetic alterations are required to potentiate LSCC, we developed a transgenic mouse to enable combined overexpression of SOX2 with deletion of distinct tumor suppressors, starting by crossing mice with inducible SOX2 and Cas9 genes (two copies, ++, each; Figure 1A). The SOX2 transgene at the *Rosa26* locus and the Cas9 at the *Hipp11* (H11) locus were both preceded by a stopper cassette (LSL) allowing the expression to be controlled via *cre*-recombinase *in vitro* and *in vivo* (Figure 1A).

Given that LSCC is thought to originate from the basal progenitor cells, we next surgically harvested the tracheal bronchial epithelium from adult SOX2;Cas9 mice and derived organoid cultures after tissue dissociation (Figure 1A). To determine the efficiency of conditionally overexpressing SOX2, we treated organoids with lentivirus containing *cre*-recombinase *in vitro*. As shown in Figure 1B and C, treatment with *cre* induced protein expression of SOX2 and SOX2-fused GFP, as seen by immunoblot and

immunohistochemical analyses (IHC). Transfected organoids express basal cell-specific markers such as cytokeratin 5 (CK5), p63, and EpCAM (Figure 1C).

Using the Consortium of Genomic Analysis (TCGA) data from LSCC cohort, we next selected the top three tumor suppressor genes (*TP53*, *PTEN* and *CDKN2A/p16*) most frequently co-mutated with *SOX2* amplification in human LSCC (Figure 1D–E). As shown in Figure 1E, we constructed lentiviral expression vectors with sgRNAs targeting one to three distinct tumor suppressors to establish different genotypes of CRISPR-mutant organoids, herein defined as control (sgLacZ), double mutant (sgp53;sgp16) and triple mutant (sgp53;sgp16;sgPten). We recognized that alternative splicing of exon 1 in *CDKN2A* could lead to two isoforms, p16 and p19(ARF), therefore, we specifically designed our guide to disrupt both isoforms. Lentiviral infection of organoids did not alter the morphology of the organoid cultures compared to controls, but we did observe a modest growth advantage in the double and triple mutant organoids (Figure 1F and Figure S2A). In order to reflect a realistic microanatomy of the tissue and to avoid potential clonal effects, our organoids were comprised of mixed multipotent progenitor cell types under puromycin selection. Sanger and whole exome sequencing of organoids confirmed mutations in the targeted genes (Figure 1G, Figure S2B, and Table S2) and immunoblotting confirmed that targeted proteins were indeed downregulated compared to control organoids (Figure 1H). Furthermore, given that Pten is a negative regulator of PI3K signaling, we assessed whether loss of Pten resulted in upregulation of the PI3K pathway. As shown in Figure 1H, immunoblotting showed increased phosphorylation of AKT at serine 473, indicating AKT pathway activation.

We next implanted transduced organoid cells into flanks of immunodeficient nude mice (Nu/Nu) and sequentially harvested tumors over a course of 96 days to evaluate tumor latency and disease progression (Figure 1I and J). After 12 weeks *in vivo*, none of the lacZ control organoids formed tumors. The double mutant organoids initially grew small tumors, but this growth eventually stalled. In early stage cases, the triple mutant organoids formed cilia, a feature seen in lung epithelia, and at week 3, tumors grew significantly and progressively larger compared to controls (Figure 1J). Hematoxylin and eosin (H&E) staining confirmed that all the double mutant tumors were benign, while triple mutant tumors harvested after day 68 formed well-differentiated squamous cell carcinomas (Figure 1J–K). SOX2 protein levels in triple mutant tumor cell lines were indeed elevated relative to human LSCC tumor cell lines (Figure 1L). We also observed some cases of adeno-squamous cell carcinomas and well-differentiated adenocarcinomas arising from the triple mutants at earlier harvests (Figure S2C). We and others have previously observed that *LKB1*-deficient ADC can progressively transdifferentiate into SCC in mouse models (10, 11), but further studies will be needed to understand whether tumors are arising from multipotent cells that transition between ADC and SCC or through selective redifferentiation within squamous carcinoma.

To confirm the phenotype of the LSCC triple mutant tumors, we further performed immunohistochemistry (IHC) for markers used clinically to distinguish human lung SCC from ADC. Similar to the human SCC samples, the LSCC triple mutant tumors displayed positive staining of p63, CK5, and SOX2 (Figure 1M and S2D). Triple mutant tumors recapitulated the hallmarks and pathology of human LSCC: squamous cells grew in solid

configurations with aberrant nuclear morphology, infiltrating neutrophils, and invading stroma with prominent keratin pearls (Figure 1K and M). We also confirmed that our LSCC model recapitulates features of the human disease transcriptionally utilizing bulk RNAseq. Prior TCGA studies on human LSCC have shown significant alternations in innate immune transcriptional networks, including HLA gene complex regulation, that are not observed in KRAS oncogene-driven LADC (11–13). Intriguingly, we found significant enrichment for innate immune and infectious disease gene sets, including viral infection response and antigen processing, in JH716 tumors relative to the well-established *KRAS*^{G12C}*;TP53* lung adenocarcinoma model (Table S5 and Figure S3A).

Cytokine profiling of conditioned media from *ex vivo* 3-dimensional (3D) culturing of double- and triple-mutant tumors after 72 hours revealed increased levels of neutrophil regulators (CXCL1, G-CSF, and GM-CSF) in SCC tumors compared to benign double mutant tumors, supporting our observation of neutrophil infiltration (CD11b^{+}/MHCII^{-}/Ly6G^{+}/Ly6C^{lo}) (Figure S3B). Lastly, we generated a stable LSCC cell line (JH716) and orthotopically implanted these lines back into littermates (Cas9;SOX2) via intra-tracheal injection to generate immunocompetent LSCC models. Immune profiling analysis demonstrated a similar percentage of tumor lymphocyte infiltration compared to our KRAS-driven genetically modified mouse models, but higher levels of myeloid CD11b^{+} cell populations (Figure S3C). LSCC phenotype was indeed preserved in tumors derived from these models and serially passaged *in vivo* to generate subsequent cell lines such as JH716–18 (Figure S3D). Taken together, these data indicate that the triple mutant tumors (*SOX2, TP53, PTEN* and *CDKN2A/p16*) strongly resembled human LSCC.

WEE1 inhibition induces DSB-stimulated type I interferon signaling and expression of genes encoding antigen-presenting MHC class I in mouse- and patient-derived lung cancer cells

Given the recent clinical response and FDA-approval for the combination of anti-PD-1 with chemotherapy as a first-line treatment of NSCLC patients, we reasoned that the DNA repair machinery is an underlying critical component that triggers anti-PD-1 response in lung cancer. We previously demonstrated that a selective small-molecule WEE1 kinase inhibitor potently induces DNA double-stranded break (DSB) formation leading to cell death in *KRAS*-mutant lung adenocarcinomas. We therefore first assessed the tumor-intrinsic cytotoxic impact of WEE1 inhibition (AZD1775) in our new squamous models (JH716) and patient-derived xenograft LSCC tumor cells (PDX139 and PDX267) along with matched normal mouse fibroblasts (JH716F) or non-tumorigenic human bronchial epithelial (HBE4 and BEAS2B) cells derived from primary lung tissues (Figure 2A and B). AZD1775 reduced cell proliferation in all lines tested but to a greater extent in tumor cells compared to normal cells (IC50s: 300 nM versus >1310nM). As expected, confocal microscopy confirmed that AZD1775 induced DSB formation as indicated by high levels of DSB marker γH2AX in treated-JH716 and PDX267 cells, supporting previous studies demonstrating cell death due to accumulation of DNA damage from mitotic catastrophe (Figure 2C). Immunoblot analyses confirmed downstream target engagement (reduced phosphorylation of CDK1 at the inhibitory tyrosine 15 site and γH2AX upregulation in a dose- and time-dependent

manner) in murine JH716 and human PDX267 cells treated with vehicle (DMSO) or AZD1775 (Figure 2D and S4A–B).

Inhibition of CDK1 has been shown to block mitotic entry and STAT1 activation (5). To investigate whether WEE1 inhibition increases STAT1 signaling by inducing CDK1 activation, we measured STAT1 phosphorylation at tyrosine 701 (pSTAT1 Y701) in mouse tumor cells treated with AZD1775 over a 24-hour time course. Activation of pSTAT1 Y701 was observed in the treated AZD1775 cells after 24-hours, and this was correlated with reduced phosphorylation of CDK1 on the inhibitory residue Y15 and elevated γH2AX, suggesting that WEE1 inhibition may be promoting DSB-induced STAT1 activation via CDK1 activation (Figure 2E). Given that STAT1 is a critical downstream transcription factor for type I interferon (IFN) signaling, we next examined the expression of IFN-stimulated genes (ISGs), such as *IFNB1, OAS1, CCL5, IFITM1, IFIT3, CDKN1A, CCL2, ISG54, and IFNA13.* Consistent with STAT1 activation, expression of ISGs was significantly upregulated in both AZD1775-treated mouse and human LSCC lines (JH716, H157, PDX277 and H520; Figure 2F–G and S5A–B) compared to controls. Similar trends were observed when cells were treated with additional small molecule WEE1 inhibitors, Wee1_II (on JH716 cells; Figure 2F), and PD0166285 (on H157 and H226 cells; Figure 2G–H) suggesting that these were ‘on-target’ effects. In addition, H226 and H157 cells were transduced with lentivirus containing short-hairpin RNA (shRNA) against WEE1 to significantly downregulate WEE1 transcript levels by 51–93% compared to cells transfected with control vector (Figure 2I). Total RNA from cells were extracted three days after transfection to assess ISG expression levels. WEE1 downregulation significantly correlated with elevated ISGs as shown in Figure 2I and S5C.

Importantly, we observed increased expression of genes encoding antigen-presenting mouse major histocompatibility complex (MHC) class I molecules (*H2K1* and *B2M*), peptide transporters (*TAP1* and *TAP2*), peptide cleavers (*ERAP1*), and transporter-MHC interactors (*TAPBP*) in JH716 cells after WEE1 inhibition (Figure 2F, right). AZD1775 treatment *in vitro* also significantly increased expression of orthologous genes in human lung cancer lines (H157, PDX277 and H520; Figure 2G right panel and S5A–B). Flow cytometry analysis showed that 72-hour treatment of AZD1775 or PD0166285 at 600nM significantly elevated expression of H-2Kb (MHC-I) by approximately two-fold but did not change PD-L1 or I-A/I-E (MHC-II) expression levels on the surface of JH716 tumor cells (Figure 2J and S5D). As further support, the JH715 tumor cell line was generated from another of the cohort of 8 malignant tumors in Figure S2C. We confirmed JH715 cells to be a separate clonal population as it contains a different cut site in *p53 (*c.809G>A/p.Arg270His) compared to the earlier-used JH716 cell line. Consistent with our results in JH716 cells, we also observed increased expression of H-2Kb upon AZD1775 treatment *in vitro* in JH715 cells (Figure S5E).

Combined ICB and WEE1 inhibition reduces tumor growth and prolongs survival

Given that our *in vitro* data demonstrated that WEE1 inhibition can increase expression of genes encoding antigen presentation molecules on lung squamous carcinoma models, we reasoned that combining AZD1775 with anti-PD-1 may enhance tumor cell killing by

stimulating T cell activity. To test this *ex vivo*, we first cultured fresh tumoroids from subcutaneous implants of JH716 cells and another lung SCC mouse model, KLN205, in 3D microfluidic culture systems. Our previous studies demonstrated that tumoroids retain the autologous tumor-infiltrating immune cells in this short-term culture system (9, 14). We observed that both single agent AZD1775 and anti-PD-1 treatment were insufficient to induce significant cell death; however, combined anti-PD-1 and AZD1775 synergistically induced cell death in both JH716- and KLN205-derived lung squamous tumoroids by 6 days co-treatment (Figure 3A–B).

To further investigate whether the observed cell death is mediated by type-I interferon signaling, we performed a CellTiter-Glo 3D cell viability assay using neutralizing antibodies specific for mouse IFN-α/ß receptor subunit 1 (IFNAR) and an TBK1 small-molecule inhibitor (BX-795), a regulator of IFN transcription (15). The addition of anti-IFNAR and BX-795 to combined AZD1775 and ICB therapy (triple combination) significantly reduced cell death of JH716 tumoroids treated with AZD1775 and ICB ($p<0.0001$; Figure 3C).

We next examined the effects of WEE1 inhibition on tumor burden *in vivo* using a low AZD1775 dose to minimize potential off-target effects while achieving target engagement (Figure 3D). AZD1775 alone was not sufficient to reduce tumor growth in JH716 mice (Figure 3E and S6A–B). However, combined AZD1775 and anti-PD-1 treatment led to significant tumor regression compared to single agents or vehicle-treated control mice, showing 97% tumor growth inhibition and nearly 60% (3/5) complete tumor remissions (Figure 3E). JH716 tumors were sensitive to anti-PD-1 single agent treatment with 59% tumor growth inhibition, but no complete regressions were observed. Depleting anti-CD8a was administrated 7 and 1 day prior to first anti-PD-1 dose and at day 14 during treatment. Therapeutic efficacy of the combination treatment was partially lost when $CD8^+$ T cells were depleted, suggesting that that while the tumor elimination phenotype is partly T cell-dependent, there are other immune modulators contributing to complete tumor elimination (Figure 3E, n=7). We further validated whether AZD1775 complements PD-1 blockade in another myeloid-enriched syngeneic mouse model, KLN205, that is refractory to anti-PD-1 therapy and has lower tumor immune infiltrate ($CD45^+$ cells) relative to JH716 tumors (Figure S6C). Similar to JH716 tumors, we observed KLN205 models were unresponsive to AZD1775 or anti-PD-1 alone but showed significant tumor growth inhibition in the combined treatment relative to anti-PD-1 or AZD1775 monotherapy, though we did not observe complete regressions (Figure 3F).

Given the potent anti-tumor effect of combined AZD1775 and ICB therapy, we next evaluated how this compared to chemotherapy and ICB dual therapy, which is currently FDA-approved for NSCLCs. Using a secondary cell line derived from parental JH716 tumors (denoted JH716–18; Figure S3D), we repeated an independent efficacy study on JH716–18 tumors starting at a volume of ~$300mm^3$ (n=10–13 per treatment arm) with the addition of the chemotherapy (carboplatin) and a combination arm (carboplatin and anti-PD-1). Survival analysis up to terminal tumor volume (20mm length) showed significant prolonged survival of mice (with 5/13 complete tumor regressions) in the AZD1775 and anti-PD-1 combination group compared to single-agent treated arms (Figure 3G). Similarly, combined carboplatin and anti-PD-1 also achieved significant survival benefit with 6/13

complete tumor regressions, suggesting that WEE1 inhibition may have comparable anti-tumor immunity as chemotherapy in our JH716–18 models. Hematological toxicity assays and body weight analyses showed that both combination therapies were well-tolerated in mice (Figure S7A–B). Consistently, we observed that combining WEE1 inhibition with ICB therapy markedly extended survival in treated KLN205 mice (Figure 3H). Multiplexed cytokine profiling of JH716–18 tumors after 1-week of treatment revealed that co-treatment with AZD1775 and anti-PD-1 downregulated levels of G-CSF, GM-CSF, CXCL2, and CXCL1, which are neutrophil chemoattractants, and increased levels of CCL5, which may enhance NK and T cell recruitment, relative to vehicle controls (Figure 3I).

Combined ICB and WEE1 inhibition reduces tumor-associated neutrophil infiltration and enhances NK recruitment in tumors

We next sought to determine how WEE1 inhibition and combined treatment may affect the quantity and subsequent recruitment of tumor-associated immune cell populations. Using flow cytometry, we analyzed the tumor-infiltrating lymphoid and myeloid cell populations at 14 days post-treatment in JH716 mice (Figure 4A–I) and 9 days post-treatment in KLN205 mice (Figure 4J–Q). In JH716 tumor-bearing mice, we observed a significant increase in $CD8^+$ tumor-infiltrating lymphocytes (TILs) in anti-PD-1 treated tumors compared to AZD1775 alone or vehicle control (Figure 4B). Combined treatment did not further elevate $CD8^+$ TIL levels relative to anti-PD-1, but did significantly increase tumor-infiltrating NK ($CD45^+/CD3^-/CD49b^+$) cells relative to vehicle controls (Figure 4C). We also observed increased $Ki67^+$ proliferating NK cells in tumors in the combination group compared to controls (Figure 4D). In addition to its effects on the lymphoid populations, combined therapy significantly decreased the $CD11b^+$ cells, including the tumor-associated neutrophils ($CD11b^+/MHCII^-/Ly6G^+/Ly6C^{lo}$; TANs) compared to AZD1775 and isotype controls (Figure 4E–F). However, combined therapy did not significantly change the proportions of tumor-associated monocyte ($CD11b^+/MHCII^+/F4/80^-/Ly6C^+$), macrophage ($CD11b^+/MHCII^+/F4/80^+/Ly6C^-$; TAMs) or dendritic cell ($CD11b^+/MHCII^+/F4/80^-/Ly6C^-/CD11c^+$) populations in the tumor (Figure 4G–I). In KLN205 tumor-bearing mice, we also observed significantly increased $CD8^+$ TILs in the combination-treated tumors compared to anti-PD-1 and isotype controls (Figure 4J). In addition, we found significantly more proliferating NK cells in the combination group relative to the controls (Figure 4K–L). In fact, AZD1775 alone increased NK infiltration (Figure 4K). Consistent with JH716 tumors, combined therapy had no significant effects on inflamed monocytes or dendritic cells, but significantly reduced TANs in KLN205 tumors relative to isotype controls (Figure 4N–Q). Taken together, this data suggests that combining WEE1 inhibition with ICB therapy enhances anti-tumor activity by reducing tumor-associated neutrophils in myeloid-enriched tumors, which is correlated with higher levels of cytotoxic $CD8^+$ T and NK cells.

Discussion

In vivo interrogation of the function of genes implicated in tumorigenesis is limited by the resource-intensive need to generate and cross mice bearing multiple, distinct engineered inducible mutant alleles. Furthermore, these models require tissue-specific cre-drivers, which can pose challenges for squamous cancers, since tamoxifen-inducible cre

recombinase can lead to premature study terminations when mice develop skin lesions before developing tumors (16).

Since the Clevers group described the successful derivation of epithelial stem cell-based organoid long-term cultures from single $Lgr5^+$ stem cells in 2009, a plethora of different tissue organoid culture methods have been developed (17). Emerging data suggest that 3D organoid cultures can recapitulate cellular composition, structure, and signaling characteristics better than traditional 2D culture (18). Here we demonstrate a successful organoid culture approach where lung squamous cell carcinoma is induced by CRISPR-Cas9-based multiplex editing of *TP53*, *PTEN* and *CDKN2A (p16)* tumor suppressor genes in lung epithelial cells derived from a *SOX2*-conditionally expressing transgenic mouse. Subsequent transplantation to immunocompetent mice reproduced LSCC that phenotypically mimic the human disease. This system enabled rapid *in vivo* characterization of driver mutations essential to induce squamous differentiation and enabled further interrogation of immunotherapeutic combinations on a genetically-defined preclinical model. Given the capacity to generate organoid models from a variety of distinct squamous tissues (19, 20), we believe this general approach will prove robust for generating squamous cell models with varied genomic features, which will powerfully enable both fundamental mechanistic and preclinical studies.

There is a clear need to develop immune-competent murine models of lung and other SCCs. Historically, squamous NSCLC treatment was mostly limited to cytotoxic chemotherapy due to the lack of targetable aberrations. In the last five years, clinical trials have demonstrated that inhibitors of PD-1 are effective in the treatment of squamous and non-squamous NSCLC (21–23). In the CheckMate 017 trial, the overall survival for previously treated squamous-cell NSCLC patients was significantly better with nivolumab than with docetaxcel, regardless of PD-L1 expression levels (21).

Most recently, the landmark KEYNOTE-407 trial has revealed efficacious anti-tumor responses in metastatic, squamous NSCLC treated first-line with pembrolizumab and platinum-based chemotherapy combination, leading to its FDA-approval (2). Accumulating evidence suggests that chemotherapy can stimulate immunosurveillance in several ways by acting on cancer cells to: (1) increase antigen presentation, (2) induce danger signals that stimulate innate immune responses, or (3) increase susceptibility of tumor cells to be recognized and killed by immune effector cells. Cisplatin, etoposide, and paclitaxel have all been shown to induce breast cancer cells to produce IFN-ß, which in turn operates as an autocrine factor to stimulate MHC class I expression (24). Similar to the chemotherapeutics' reliance on DSB formation to drive tumor cell killing, we and others have previously shown that selective inhibition of WEE1, a negative regulator of a CDK1, leads to potent DSB formation due to exacerbated mitotic catastrophe in deregulated cancer cells (25). As such, we hypothesized that selective inhibition of WEE1 may similarly elicit tumor cell immunogenicity. Indeed, we show that AZD1775 and WEE1i treatment *in vitro* potently increases expression of antigen processing and presentation genes in both mouse and patient-derived LSCC xenograft cell lines, which correlates with DSB as measured by increased ɣH2AX foci formation in tumor cells.

Harding and colleagues previously showed that CDK1i prevented STAT1 activation in PARPi-treated BRCA1-mutated ovarian cancer cells, suggesting that mitotic entry is a gateway to inflammatory signaling for diverse DSB-inducing stimuli (5). Consistent with this, we demonstrate that activation of CDK1 by AZD1775 treatment not only induces STAT1 phosphorylation at Y701 in a time-dependent manner, but also increases ISG expression in tumor cells, likely explaining their enhanced capacity for antigen presentation (24). Along similar lines, Goel and colleagues recently showed that CDK4/6 inhibition induced cell cycle arrest that resulted in global upregulation of an IFN-driven transitional program and viral mimicry on breast cancer cells (26). Although CDK1 is best known for its role in controlling the G_2/M cell cycle checkpoint, a novel function of the kinase in immune response has emerged. For instance, Cribier and colleagues identified that CDK1 phosphorylates SAMHD1 at residue Thr592, directly inhibiting its antiviral restriction activity (27). SAMHD1 is a deoxynucleotide triphosphate (dNTP) triphosphohydrolase that reduces the intracellular pool of dNTPs to restrict HIV-1 synthesis (27). Depletion of SAMHD1 leads to enhanced antigen presentation and chronic type I IFN secretion upon HIV-1 infection and facilities T cell responses in co-culture models (28). Further studies will be necessary to carefully interrogate whether SAMHD1 or other interacting partners of CDK1 may be mediating the IFN response upon AZD1775 treatment, rendering the tumor microenvironment more permissive to T or NK cell infiltration.

Nearly all humans with LSCCs have a history of tobacco use that drives squamous metaplasia and the development of an inflammatory microenvironment and chronic immune-suppression (29). TANs and TAMs comprise a significant proportion of the inflammatory infiltrates in both mouse tumor models and human cancers (29). Here, we found that our orthotopic JH716 tumors were indeed enriched for tumor-infiltrating $CD11b^+$ myeloid cells and inflammatory cytokines compared to a well-established $KRAS^{G12D}$ lung adenocarcinoma mouse model (Figure S3C). Our *in vivo* efficacy studies demonstrate that co-treatment with anti-PD-1 and AZD1775 significantly reduces tumor growth and TAN infiltration post-combination treatment in JH716 and KLN205 tumors. Consistently, we found that treatment with AZD1775 in JH716 mice resulted in reduced levels of neutrophil chemoattractant G-CSF. Notably, the addition of anti-PD-1 therapy with AZD1775 further reduced intratumoral levels of G-CSF and CXCL2. As type I IFNs have been shown to downregulate G-CSF expression and G-CSF is known to be a major regulator of neutrophil development and mobilization, and CXCL2 secretion, we speculate that reduced neutrophil chemoattractants may be partly due to DSB-stimulated type I interferon signaling upon AZD1775 treatment (30).

Previous studies have shown that TANs can suppress T cell responses and inhibit NK cell function, establishing a pro-tumor microenvironment that facilitates metastatic formation (31). Consistently, we observed an inverse correlation between TAN abundance and increased $CD8^+$ T and NK cells in our JH716 and KLN205 tumors treated with dual therapy. In agreement with our data, De Henau and colleagues showed that targeting myeloid cells via PI3Kγ inhibition enhanced immunotherapeutic effect of anti-PD-1 in resistant tumors (32). Given that emerging data suggest that neutrophils contribute to anti-PD-1 resistance, further studies are needed to delineate the mechanistic basis of how combined anti-PD-1 and AZD1775 reduces TAN infiltration.

Previous studies have demonstrated that CDK inhibition prevents death of terminally differentiated neurons, suggesting that non-cycling cells such as neutrophils may require activation of CDK for apoptotic induction (33, 34). By contrast, others have shown that human neutrophils express CDK1, CDK2, and CDK5, and that specific inhibitors of CDKs (namely, R-roscovitine) induce caspase-dependent apoptosis (35). CDK activity is clearly important to neutrophil survival (34, 35). Thus, it would be interesting to examine whether AZD1775-induced DNA damage directly mediates neutrophil homeostasis by either deregulating signaling of its trafficking receptors (i.e., CXCR2) or apoptotic response.

In addition to the reduction of TANs, we also observed that AZD1775 combined with ICB therapy led to increased NK cell infiltration. Our cytokine profiling data showed elevated intratumoral CCL5 levels in co-treated JH716 samples, which may partially explain the heightened NK cell influx. Recently, Böttcher *et al.* demonstrated that cDC1 accumulation in mouse tumors often depends on NK cells that produce cDC1 chemoattractants CCL5 that augment immunotherapeutic response (36). Indeed, we also observed a positive correlation between intratumoral CCL5 chemokine levels and NK infiltrates. However, while we observed a trend of increased tumor-associated DCs ($CD11b^+/MHCII^+/F4/80^-/Ly6C^-/CD11c^+$) compared to controls in JH716 tumors, this did not reach significance. Further NK cell depletion studies are needed to delineate whether NK cells are directly mediating the anti-tumor effects of combined therapy or indirectly stimulating recruitment of cDC1. It is also tantalizing to speculate that we may be observing NK cell-mediated anti-tumor immunity due to WEE1 inhibitor-mediated DNA damage and subsequent STING and type I IFN pathway activation, as has been recently shown (37). Such a mechanism would be consistent with our observed NK cell accumulation and increased proliferation in our AZD1775-treated tumor models.

We have pioneered the development of *ex vivo* genomic editing of mouse 3D organoid cultures to generate a rapid, novel LSCC mouse model that exhibits characteristic histopathology and biomarker expression similar to human LSCC. We generated two cell lines, JH715 and JH716, harboring *SOX2;PTEN;CDKN2A;TP53* alterations. JH715 cells differ from JH716 by the *TP53* cut site, but also exhibited increased expression of H-2Kb upon AZD1775 treatment *in vitro*, which we believe supports the WEE1-specific immunological mechanism described in significant depth utilizing JH716 cells. We have also applied this system to explore different genotypes of human LSCC, but have observed that single or double alterations of *TP53*, *CDKN2A* or *KDM6A* in concert with SOX2 overexpression was not sufficient to form LSCC tumors, therefore limiting generation of additional mouse cells from these specific genotypes (Figure 1I and Figure S8A–D). Our work illustrates the challenges in understanding which cooperating mutations potentiate LSCC, since not all genotypes lead to LSCC in mice. Consistent with our data, Bern's group have also demonstrated that various combinations of genetic lesions can determine different cell fates and showed that *SOX2;PTEN;CDKN2A* transgenic mice gave rise to LSCC tumors in 7–9 months with a 73% penetrance, while *FGFR;PTEN;CDKN2NA* mice had 19% SCC penetrance (38). Sequencing of JH716 tumors also revealed mutations in genes not known to drive LSCC (data not shown). We believe that the combined effects of deleting genes in the DNA damage repair/cell cycle machinery during long term *in vivo* culturing leads to accumulation of passenger mutations that help facilitate rapid LSCC tumorigenesis.

Yet another possibility is the potential of Cas9-induced immunity or off-target effects, which continues to be actively investigated in this field since the full impact of pre-existing immunity has yet to be fully determined (39).

Using this mouse model, we explored a rational therapeutic combination to enhance response to PD-1 blockade by stimulating immunosurveillance with a selective DSB-inducing agent. We demonstrated for the first time that CDK1 activation via WEE1 inhibition can induce DSB-stimulated type I interferon signaling and antigen presentation in mouse and patient-derived LSCC tumors. Combined WEE1 and PD-1 inhibition significantly induced anti-tumor efficacy both *ex vivo* and *in vivo,* consistent with the efficacious response observed in mice treated with carboplatin and anti-PD1 co-treatment. While we did observe some inhibitory activity in non-transformed cells treated with AZD1775, we believe that cancer cells with high replicative stress are more vulnerable and therefore we speculate that selectively activating CDK1 by AZD1775 may minimize the off-target side effects associated with chemotherapy while augmenting anti-tumor immunity. The clinical challenge will be to assess dose-limiting toxicity associated with the promiscuous nature of kinase inhibitors such as AZD1775. In fact, phase I trials (NCT00648648) of AZD1775 and chemotherapy showed responding patients with advanced solid tumors were mildly enriched for p53 mutations (response rate of 21% and 12% in p53 mutant and p53 wild-type, respectively), supporting the notion that patient selection may be necessary to obtain the maximum benefit from AZD1775 and ICB combination therapy (40). Yet another possibility is that relapsed p53 mutant tumors relying on G_2/M checkpoint may be more responsive to AZD1775 and ICB combination therapy than tumors with intact G_1 checkpoint. Future studies may also evaluate whether triple combinations such as AZD1775, PARPi and ICB therapies targeting both G_1, G_2, and immune checkpoints may reach improved efficacy. Our observations illuminate a clinical hypothesis for combining anti-PD1 with DNA damage-inducing therapies in the treatment of LSCC. As with all preclinical model systems, prospective clinical trials will be needed to substantiate the hypothesis of our work.

Supplementary Material

Refer to Web version on PubMed Central for supplementary material.

Acknowledgements

This work was supported by the National Cancer Institute (U01 CA233084-01 (Co-PI), CA213333 (PI), R01 CA219670-A1 (Co-PI), CA216188-01A1 (Co-PI), CA222218-01A1 (Co-I), CA205150 (Co-I), CA201049 (Co-I), CA197329 (Co-I), CA140594 (PI), CA166480 (Co-I), P01 CA098101 (PI) and CA154303 (Co-I)) to K.K.W and CA187119 to A.J.B.

The authors thank Mei Zhang (BWH) for help with immunohistochemistry work, Yanxi Zhang (DFCI) and Xiaoen Wang (DFCI) for technical animal assistance, Dr. Elena Ivanova (Belfer Center) for technical help and protocols for staining 3D cultures and Dr. Israel Canadas (DFCI) for thoughtful discussions about innate pathway signaling. We thank Drs. Joe Wang, Limei Ouyang and Elinor Sun from the BGI Group for whole-exome sequencing and RNAseq analysis.

Competing interests: KKW is a co-founder of G1 Therapeutics and is a consultant for AstraZeneca, Janssen, Pfizer, Array, Novartis, Merck, Takeda, Ono and Bristol-Myers Squibb. AJB receives research funding from Merck, Bayer and Novartis and is a co-founder of Signet Therapeutics. LMS is a consultant for AstraZeneca, LOXO Oncology, and Foghorn Therapeutics. All other authors have no conflicts of interest.

References

1. Huang Q, Zhang H, Hai J, Socinski MA, Lim E, Chen H, et al. Impact of PD-L1 expression, driver mutations and clinical characteristics on survival after anti-PD-1/PD-L1 immunotherapy versus chemotherapy in non-small-cell lung cancer: A meta-analysis of randomized trials. OncoImmunology. 2017:e1396403.
2. Paz-Ares L, Luft A, Vicente D, Tafreshi A, Gumus M, Mazieres J, et al. Pembrolizumab plus Chemotherapy for Squamous Non-Small-Cell Lung Cancer. The New England journal of medicine. 2018;379:2040–51. [PubMed: 30280635]
3. Zitvogel L, Galluzzi L, Smyth MJ, Kroemer G. Mechanism of action of conventional and targeted anticancer therapies: reinstating immunosurveillance. Immunity. 2013;39:74–88. [PubMed: 23890065]
4. Peng J, Hamanishi J, Matsumura N, Abiko K, Murat K, Baba T, et al. Chemotherapy Induces Programmed Cell Death-Ligand 1 Overexpression via the Nuclear Factor-kappaB to Foster an Immunosuppressive Tumor Microenvironment in Ovarian Cancer. Cancer research. 2015;75:5034–45. [PubMed: 26573793]
5. Harding SM, Benci JL, Irianto J, Discher DE, Minn AJ, Greenberg RA. Mitotic progression following DNA damage enables pattern recognition within micronuclei. Nature. 2017;548:466–70. [PubMed: 28759889]
6. Hai J, Liu S, Bufe L, Do K, Chen T, Wang X, et al. Synergy of WEE1 and mTOR Inhibition in Mutant KRAS-Driven Lung Cancers. Clinical Cancer Research. 2017;23:6993–7005. [PubMed: 28821559]
7. Lu Y, Futtner C, Rock JR, Xu X, Whitworth W, Hogan BL, et al. Evidence that SOX2 overexpression is oncogenic in the lung. PloS one. 2010;5:e11022. [PubMed: 20548776]
8. John T, Kohler D, Pintilie M, Yanagawa N, Pham NA, Li M, et al. The ability to form primary tumor xenografts is predictive of increased risk of disease recurrence in early-stage non-small cell lung cancer. Clinical Cancer Research. 2011;17:134–41. [PubMed: 21081655]
9. Jenkins RW, Aref AR, Lizotte PH, Ivanova E, Stinson S, Zhou CW, et al. Ex Vivo Profiling of PD-1 Blockade Using Organotypic Tumor Spheroids. Cancer discovery. 2018;8:196–215. [PubMed: 29101162]
10. Hou S, Zhou S, Qin Z, Yang L, Han X, Yao S, et al. Evidence, Mechanism, and Clinical Relevance of the Transdifferentiation from Lung Adenocarcinoma to Squamous Cell Carcinoma. The American journal of pathology. 2017;187:954–62. [PubMed: 28284717]
11. Xu C, Fillmore CM, Koyama S, Wu H, Zhao Y, Chen Z, et al. Loss of Lkb1 and Pten leads to lung squamous cell carcinoma with elevated PD-L1 expression. Cancer cell. 2014;25:590–604. [PubMed: 24794706]
12. Comprehensive genomic characterization of squamous cell lung cancers. Nature. 2012;489:519–25. [PubMed: 22960745]
13. Comprehensive molecular profiling of lung adenocarcinoma. Nature. 2014;511:543–50. [PubMed: 25079552]
14. Deng J, Wang ES, Jenkins RW, Li S, Dries R, Yates K, et al. CDK4/6 Inhibition Augments Antitumor Immunity by Enhancing T-cell Activation. Cancer discovery. 2018;8:216–33. [PubMed: 29101163]
15. Sheehan KC, Lai KS, Dunn GP, Bruce AT, Diamond MS, Heutel JD, et al. Blocking monoclonal antibodies specific for mouse IFN-alpha/beta receptor subunit 1 (IFNAR-1) from mice immunized by in vivo hydrodynamic transfection. Journal of Interferon & cytokine research. 2006;26:804–19. [PubMed: 17115899]
16. Brocard J, Warot X, Wendling O, Messaddeq N, Vonesch JL, Chambon P, et al. Spatio-temporally controlled site-specific somatic mutagenesis in the mouse. Proceedings of the National Academy of Sciences of the United States of America. 1997;94:14559–63. [PubMed: 9405652]
17. Sato T, Vries RG, Snippert HJ, van de Wetering M, Barker N, Stange DE, et al. Single Lgr5 stem cells build crypt-villus structures in vitro without a mesenchymal niche. Nature. 2009;459:262–5. [PubMed: 19329995]

18. Clevers H Modeling Development and Disease with Organoids. Cell. 2016;165:1586–97. [PubMed: 27315476]
19. Kijima T, Nakagawa H, Shimonosono M, Chandramouleeswaran PM, Hara T, Sahu V, et al. Three-Dimensional Organoids Reveal Therapy Resistance of Esophageal and Oropharyngeal Squamous Cell Carcinoma Cells. Cellular and molecular gastroenterology and hepatology. 2019;7:73–91. [PubMed: 30510992]
20. Driehuis E, Kolders S, Spelier S, Lohmussaar K, Willems SM, Devriese LA, et al. Oral Mucosal Organoids as a Potential Platform for Personalized Cancer Therapy. Cancer discovery. 2019;9:852–71. [PubMed: 31053628]
21. Brahmer J, Reckamp KL, Baas P, Crino L, Eberhardt WE, Poddubskaya E, et al. Nivolumab versus Docetaxel in Advanced Squamous-Cell Non-Small-Cell Lung Cancer. The New England journal of medicine. 2015;373:123–35. [PubMed: 26028407]
22. Reck M, Rodriguez-Abreu D, Robinson AG, Hui R, Csoszi T, Fulop A, et al. Pembrolizumab versus Chemotherapy for PD-L1-Positive Non-Small-Cell Lung Cancer. The New England journal of medicine. 2016;375:1823–33. [PubMed: 27718847]
23. Herbst RS, Baas P, Kim DW, Felip E, Perez-Gracia JL, Han JY, et al. Pembrolizumab versus docetaxel for previously treated, PD-L1-positive, advanced non-small-cell lung cancer (KEYNOTE-010): a randomised controlled trial. Lancet (London, England). 2016;387:1540–50.
24. Wan S, Pestka S, Jubin RG, Lyu YL, Tsai YC, Liu LF. Chemotherapeutics and radiation stimulate MHC class I expression through elevated interferon-beta signaling in breast cancer cells. PloS one. 2012;7:e32542. [PubMed: 22396773]
25. Pfister SX, Markkanen E, Jiang Y, Sarkar S, Woodcock M, Orlando G, et al. Inhibiting WEE1 Selectively Kills Histone H3K36me3-Deficient Cancers by dNTP Starvation. Cancer cell. 2015;28:557–68. [PubMed: 26602815]
26. Goel S, DeCristo MJ, Watt AC, BrinJones H, Sceneay J, Li BB, et al. CDK4/6 inhibition triggers anti-tumour immunity. Nature. 2017;548:471–5. [PubMed: 28813415]
27. Cribier A, Descours B, Valadao AL, Laguette N, Benkirane M. Phosphorylation of SAMHD1 by cyclin A2/CDK1 regulates its restriction activity toward HIV-1. Cell reports. 2013;3:1036–43. [PubMed: 23602554]
28. Maelfait J, Bridgeman A, Benlahrech A, Cursi C, Rehwinkel J. Restriction by SAMHD1 Limits cGAS/STING-Dependent Innate and Adaptive Immune Responses to HIV-1. Cell reports. 2016;16:1492–501. [PubMed: 27477283]
29. Kargl J, Busch SE, Yang GH, Kim KH, Hanke ML, Metz HE, et al. Neutrophils dominate the immune cell composition in non-small cell lung cancer. Nature communications. 2017;8:14381.
30. Wu CF, Andzinski L, Kasnitz N, Kroger A, Klawonn F, Lienenklaus S, et al. The lack of type I interferon induces neutrophil-mediated pre-metastatic niche formation in the mouse lung. International journal of cancer. 2015;137:837–47. [PubMed: 25604426]
31. Spiegel A, Brooks MW, Houshyar S, Reinhardt F, Ardolino M, Fessler E, et al. Neutrophils Suppress Intraluminal NK Cell-Mediated Tumor Cell Clearance and Enhance Extravasation of Disseminated Carcinoma Cells. Cancer discovery. 2016;6:630–49. [PubMed: 27072748]
32. De Henau O, Rausch M, Winkler D, Campesato LF, Liu C, Cymerman DH, et al. Overcoming resistance to checkpoint blockade therapy by targeting PI3Kgamma in myeloid cells. Nature. 2016;539:443–7. [PubMed: 27828943]
33. Modi PK, Komaravelli N, Singh N, Sharma P. Interplay between MEK-ERK signaling, cyclin D1, and cyclin-dependent kinase 5 regulates cell cycle reentry and apoptosis of neurons. Molecular biology of the cell. 2012;23:3722–30. [PubMed: 22833568]
34. Monaco EA 3rd, Vallano ML. Cyclin-dependent kinase inhibitors: cancer killers to neuronal guardians. Current medicinal chemistry. 2003;10:367–79. [PubMed: 12570697]
35. Rossi AG, Sawatzky DA, Walker A, Ward C, Sheldrake TA, Riley NA, et al. Cyclin-dependent kinase inhibitors enhance the resolution of inflammation by promoting inflammatory cell apoptosis. Nature medicine. 2006;12:1056–64.
36. Bottcher JP, Bonavita E, Chakravarty P, Blees H, Cabeza-Cabrerizo M, Sammicheli S, et al. NK Cells Stimulate Recruitment of cDC1 into the Tumor Microenvironment Promoting Cancer Immune Control. Cell. 2018;172:1022–37.e14. [PubMed: 29429633]

37. Marcus A, Mao AJ, Lensink-Vasan M, Wang L, Vance RE, Raulet DH. Tumor-Derived cGAMP Triggers a STING-Mediated Interferon Response in Non-tumor Cells to Activate the NK Cell Response. Immunity. 2018;49:754–63.e4. [PubMed: 30332631]

38. Ferone G, Song JY, Sutherland KD, Bhaskaran R, Monkhorst K, Lambooij JP, et al. SOX2 Is the Determining Oncogenic Switch in Promoting Lung Squamous Cell Carcinoma from Different Cells of Origin. Cancer cell. 2016;30:519–32. [PubMed: 27728803]

39. Crudele JM, Chamberlain JS. Cas9 immunity creates challenges for CRISPR gene editing therapies. Nature communications. 2018;9:3497.

40. Leijen S, van Geel RM, Pavlick AC, Tibes R, Rosen L, Razak AR, et al. Phase I Study Evaluating WEE1 Inhibitor AZD1775 As Monotherapy and in Combination With Gemcitabine, Cisplatin, or Carboplatin in Patients With Advanced Solid Tumors. Journal of Clinical Oncology. 2016;34:4371–80. [PubMed: 27601554]

Translational Relevance

Considering the absence of targeted therapies for LSCC, the generation of clinically-relevant preclinical mouse models is urgently needed. Here, we generated a novel mouse model that represents the most frequent aberrations found in human LSCC, serving as an invaluable tool for developing better immunotherapeutic combinatorial strategies to treat patients.

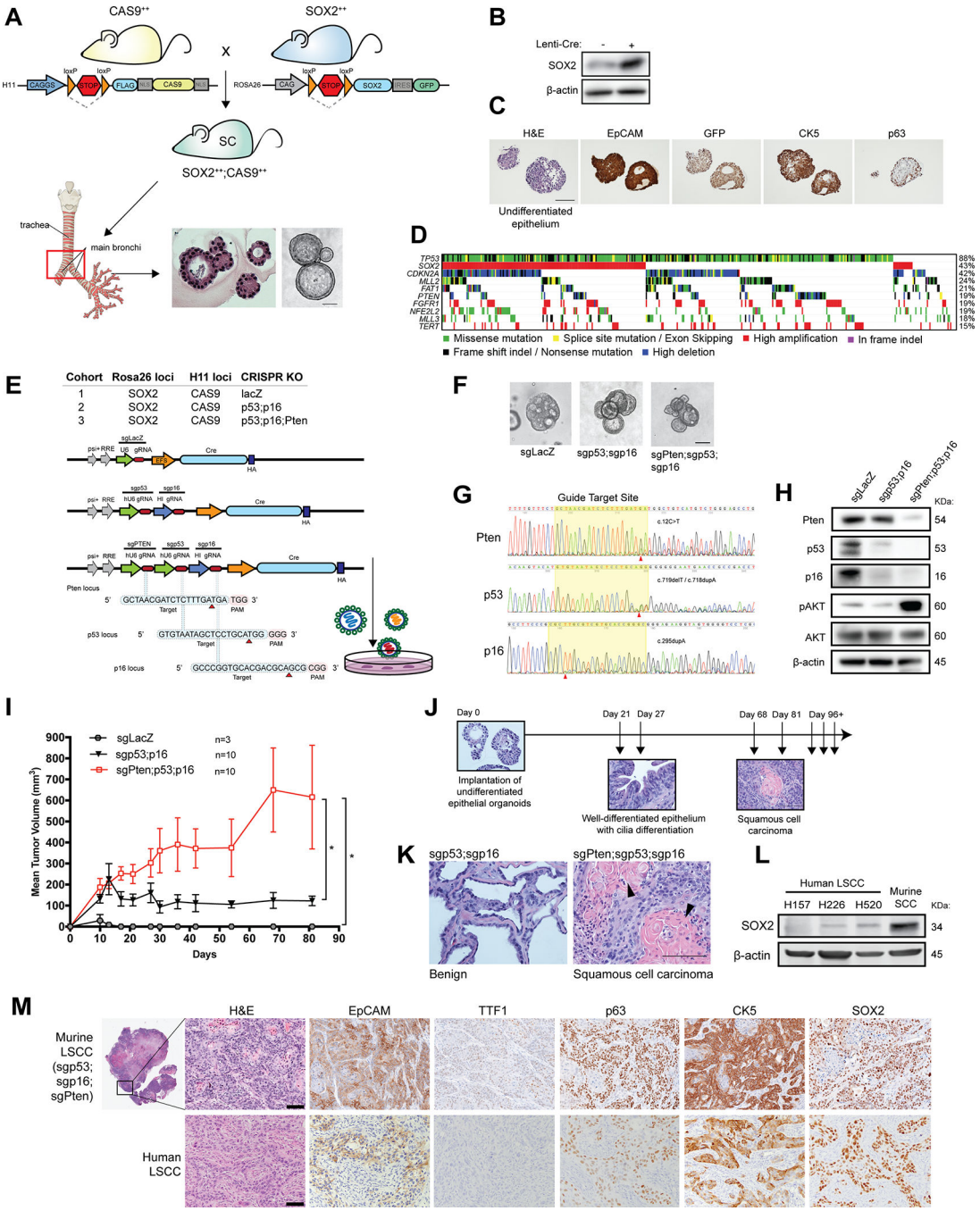

Figure 1. Generation of CRISPR-mutant organoids that give rise to lung squamous carcinoma.

A. Generation of *cre*-inducible SOX2^{++};Cas9^{++} mice. The Rosa26R-lox-stop-lox-Sox2-IRES-GFP mice (SOX2) was bred with H11-lox-stop-lox-Cas9 (Cas9) mice to obtain a SOX2;Cas9 colony. The SOX2 and Cas9 gene at Rosa26 and H11 loci, respectively, are preceded by a stopper cassette allowing the expression to be controlled via *cre* recombinase. Organoids were derived from the tracheal bronchial of mouse lungs where human LSCC most frequently occurs**. B.** Immunoblot analyses indicate that SOX2 protein levels are elevated compared to controls when transfected with lentivirus containing *cre*. **C.**

Immunohistochemistry (IHC) analyses demonstrate that transfected organoids express basal cell-specific markers such as keratin 5 (CK5), p63 and EpCAM. Organoids displayed undifferentiated epithelial phenotype *in vitro*. GFP reporter activity is detected only after *cre*-mediated recombination of the LoxP sites as demonstrated by treating organoids with lentivirus containing *Cre*. **D.** Integrated view of the top 10 most frequent genomic aberrations in The Cancer Genome Atlas (TCGA) data in LSCC tumors. **E.** Three different genotypes of mutant organoids were generated using three lentiviral constructs containing sgRNAs targeting *Pten, p53, p16,* and *LacZ* control. **F**. Representative images depicting transfected organoids. **G.** Representative chromatogram sequences of *Pten (*c.12C>T*), p53* (c.719delT/c.718dupA) and *p16* (c.295dupA) loci in triple-mutant organoids. **H**. Immunoblot analyses demonstrate decreased levels of target proteins relative to control. **I.** Two million CRISPR-mutant organoids were implanted into nude mice to assess tumorigenicity. P value was determined by unpaired t-test. **J.** Tumors were assessed sequentially to evaluate tumor progression. Representative haematoxylin and eosin (HE)-stained sections of harvested tumors. **K.** Representative HE-stained sections showing the difference between tumors derived from sgp53;sgp16 and sg53;sgp16;sgPten implanted organoids. **L**. Immunoblot analysis compared SOX2 expression in human ATCC LSCC cell lines with our mouse SCC cells. **M.** Immunohistochemistry analyses showed that SCC tumors from triple-mutant organoids resembled the human LSCC, expressing the classic squamous markers, p63 and cytokeratin 5 seen in human disease and the hallmarks of squamous differentiation such as keratin deposition. Scale bar, 100μm.

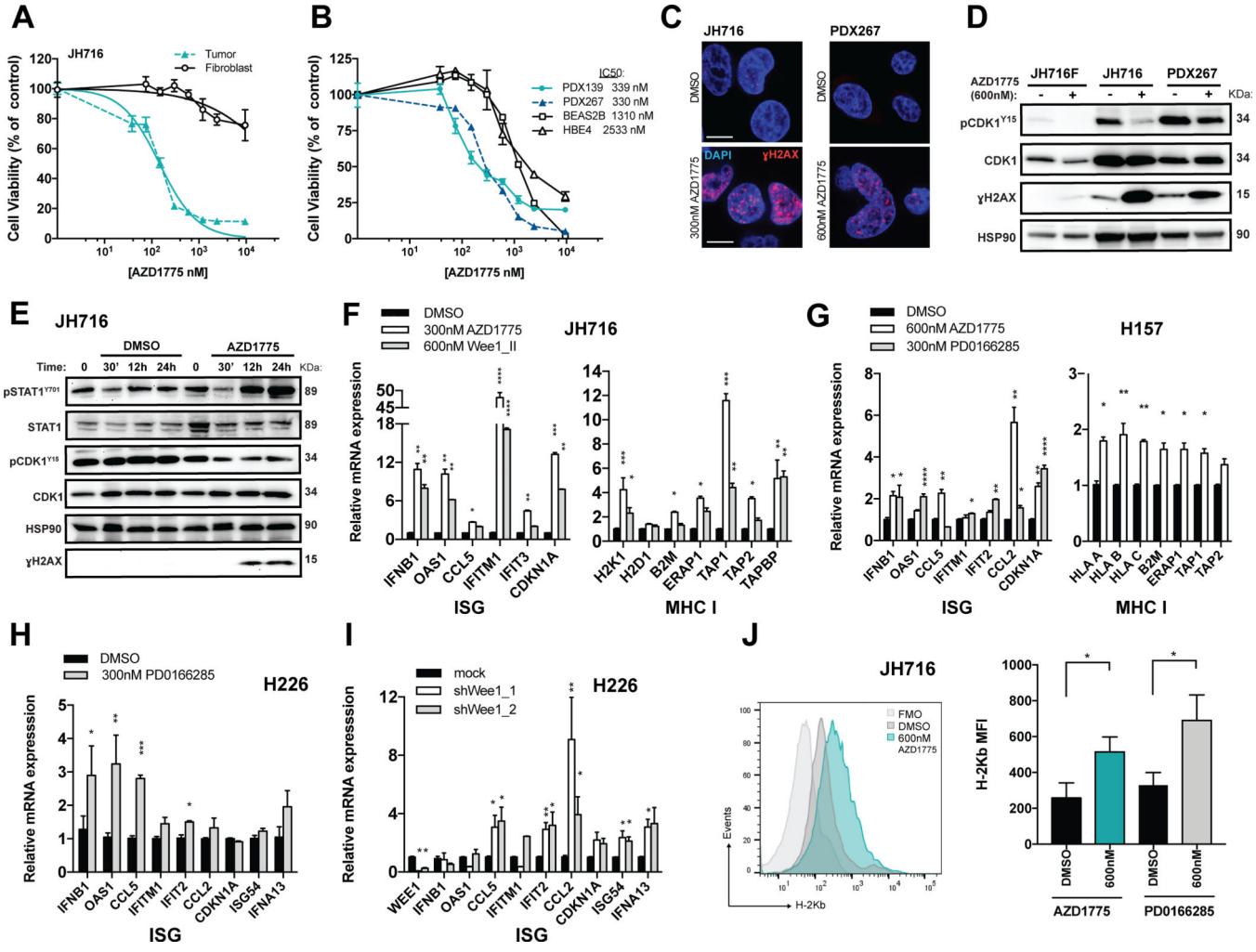

Figure 2. WEE1 inhibition induces DNA damage, activating STAT1 signaling and stimulating expression of type I interferon and antigen presentation gene in murine and patient-derived LSCC cell lines.

A. Dose-response curves of murine JH716 tumor cells and matched fibroblast cells treated for three days with AZD1775. **B.** Dose-response curves of patient-derived xenograft LSCC cells (PDX139 and PDX267) and normal epithelial lung cells (HBE4 and BEAS2B) treated for three days with AZD1775. **C.** Detection of γH2AX and DAPI in JH716 (left panel) and PDX267 (right panel) cells by immunofluorescence after 48 hours treatment with vehicle (DMSO) or AZD1775 (300 and 600nM, respectively). Representative foci-containing cells at high-power magnification are shown. **D.** To assess downstream target engagement (pCDK1 at tyrosine 15 and γH2AX) in murine JH716 and patient-derived LSCC PDX267 cells, immunoblot analyses were performed on whole-cell lysates 48 hours after treatment with vehicle (DMSO) or AZD1775 (600nM). **E.** Representative immunoblot for activation of STAT1 signaling at indicated times after 600nM AZD1775 treatment on JH716 cells. **F and G.** qRT-PCR analysis was used to measure mRNAs of type I IFN-stimulated genes (ISG) and antigen presentation genes in murine LSCC JH716 cells (**F**) and human LSCC H157 and H226 cells (**G-H**) treated with small molecule WEE1 inhibitors (AZD1775, Wee1_II, or PD0166285) for 24 hours. **I.** WEE1 transcript levels were downregulated in

H226 cells using two different shRNAS targeting WEE1 and a pLKO. empty vector control. mRNA of ISGs were measured by qRT-PCR analysis three days after transduction. **J.** Expression of H-2Kb on JH716 cells treated with AZD1775 (600nM) or PD0166285 (600nM) for three days. Quantification of mean fluorescence intensity (MFI) is shown in the right. FMO indicates fluorescence minus one. Data are shown as mean ±SEM. P values were determined by Kruskal-Wallis test (n=4 biological replicates; *p<0.05. **p<0.01, ***p<0.001).

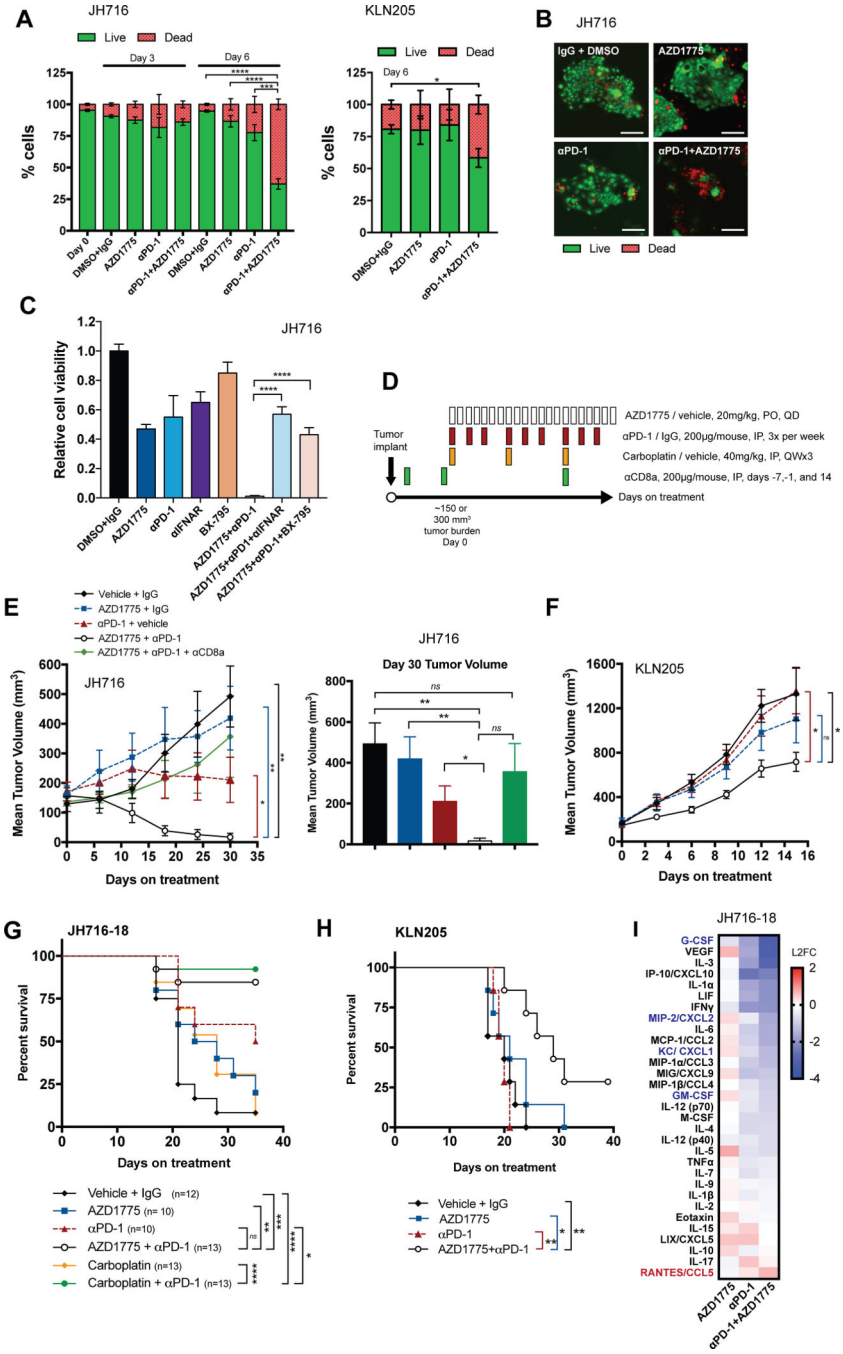

Figure 3. Combined ICB and WEE1 inhibition reduces tumor growth and prolongs survival

A. Quantification results of live (AO=green) and dead (PI=red) analysis of LSCC tumoroids (JH716 and KLN205) cultured in 3D microfluidic culture at day 0, day 3 and day 6 following treatment of AZD1775 (300nM) alone or in combination with PD-1 antibody (10μg/mL) as indicated (n=3 biological replicates). **B**. Representative images of deconvoluted fluorescence microscopy shows live/dead stained JH716 cells at day 6 after indicated treatment. Statistical analysis was calculated by comparing each group with the combination group treated at day 6 by one-way ANOVA. **C.** CellTiter-Glo 3D cell viability

assays using neutralizing antibodies specific for mouse IFN-α/ß receptor subunit 1 (IFNAR;40μg/mL) and a TBK1 small-molecule inhibitor (BX-795;1μM) was performed on JH716 tumoroids treated with AZD1775 (300nM) and anti-PD-1 (10μg/mL) for 7 days. Quantification of mean luminescence was normalized to vehicle controls as shown. P values were determined by one-way ANOVA (n=3 biological replicates). **D.** Therapy regimen (PO, *per os*, IP, intraperitoneal, QD, once a day, QW, once a week). **E-F.** Mean tumor volume of subcutaneous JH716 (n=5–7/group) (**E**) and KLN205 (n=7/group) (**F**) implants in mice treated with vehicle, AZD1775, anti-PD-1, or in combination when tumor burden reached ~150mm^3. **G-H.** Survival analysis was performed on an independent JH716–18 tumor efficacy study at ~300mm^3 consisting of n=10–13 animals per group (**G**) and KLN205 tumors consisting of n=7 animals per group from F (**H**). **I.** Heat map of intratumoral cytokine profiles from JH716–18 tumors treated for 1-week are expressed as $\log_2$ fold change (L2FC) relative to vehicle controls (n=5–7 tumors per group). Data are shown as mean ±SEM (*p<0.05. **p<0.01, ***p<0.001, ****p<0.0001). A log-rank Mantel-Cox test was used for Kaplan-Meier analysis. Scale bar, 100μm.

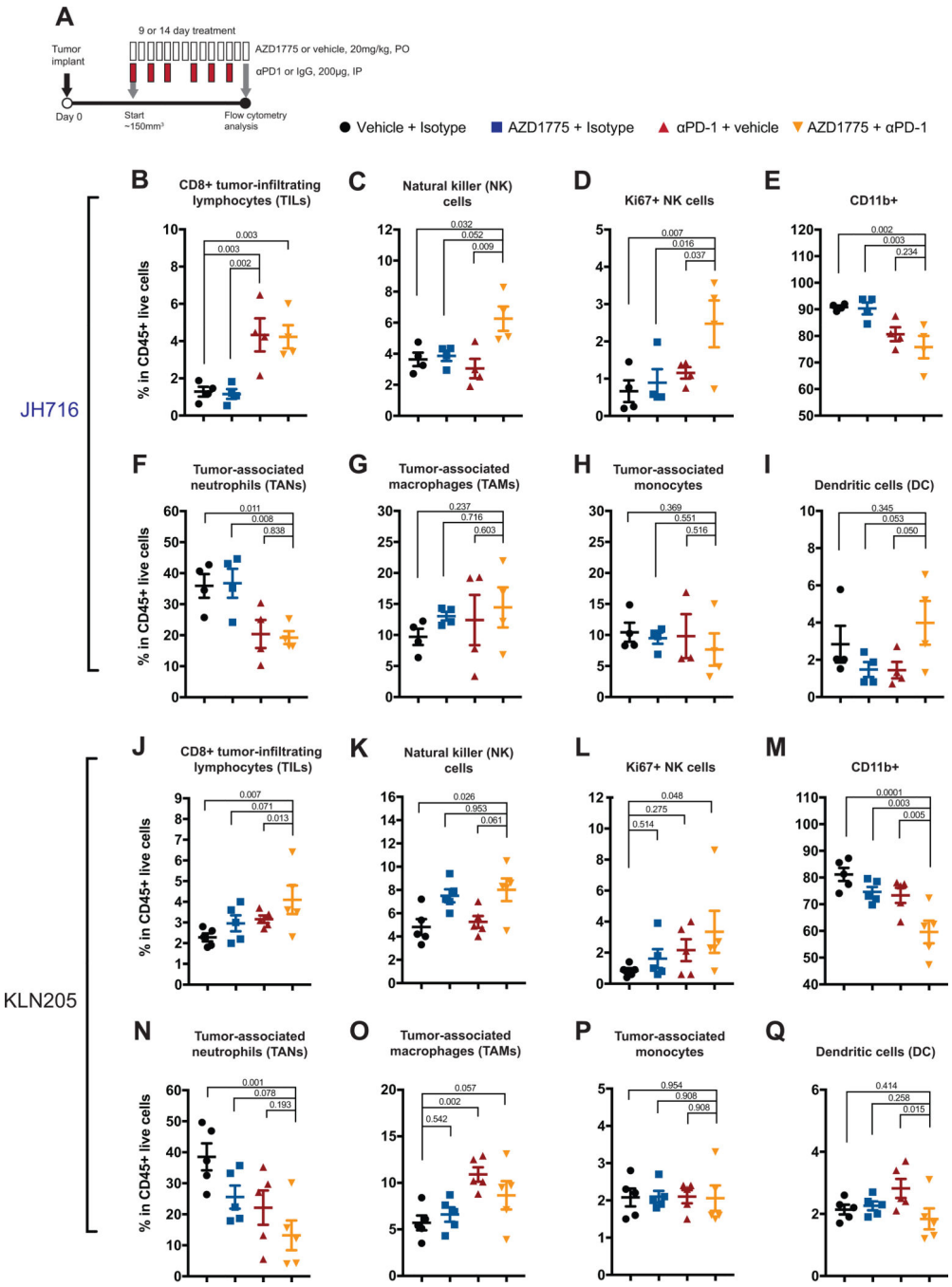

Figure 4. Phenotyping of tumor-associated immune cell populations after treatment in JH716 and KLN205 mouse models

A. Therapy regimen and flow cytometry analysis time points (PO, *per os*, QD, once a day, IP, intraperitoneal). Mice were subcutaneously inoculated with JH716 (3×10^6) and KLN205 (0.5×10^6) cells and treated with vehicle, AZD1775 (20mg/kg), anti-PD-1(200μg), or combination therapy for 14 and 9 days, respectively. **B-F**. Quantification by flow cytometry of (**B**) $CD8^+$ T cells, (**C**) Natural killer cells (NK), (**D**) $Ki67^+$ proliferating NK cells, (**E**) $CD11b^+$ myeloid cells, (**F**) Tumor associated-neutrophils (TANs; $CD11b^+/MHCII^-/Ly6G^+/$

Ly6C^{lo}), (**G)** Tumor-associated macrophages (TAM; CD11b^{+}/MHCII^{+}/F4/80^{+}/Ly6C^{-}), (**H**) Tumor-associated monocytes (CD11b^{+}/MHCII^{+}/F4/80^{-}/Ly6C^{+}), (**I**) Tumor-associated dendritic cells (CD11b^{+}/MHCII^{+}/F4/80^{-}/Ly6C^{-}/CD11c^{+}), in CD45^{+} TILs from dissociated JH716 tumors. **J-Q**. Flow cytometry analysis of dissociated KLN205 tumors. Each data point represents one mouse (n=4–5 mice per group). P values were determined by one-way ANOVA analyses. Data are shown as mean ±SEM.